JACS Au
AN OPEN ACCESS JOURNAL OF THE AMERICAN CHEMICAL SOCIETY

Editors' Choice
Open Access

pubs.acs.org/jacsau

Article

Lanthanide-Dependent Photochemical and Photophysical Properties of Lanthanide−Anthracene Complexes: Experimental and Theoretical Approaches

Liangliang Wu,[⊥] Xin-Da Huang,[⊥] Weijia Li,[⊥] Xiaoyan Cao, Wei-Hai Fang, Li-Min Zheng,* Michael Dolg,* and Xuebo Chen*

Cite This: *JACS Au* 2024, 4, 3606−3618

Read Online

ACCESS | Metrics & More | Article Recommendations | Supporting Information

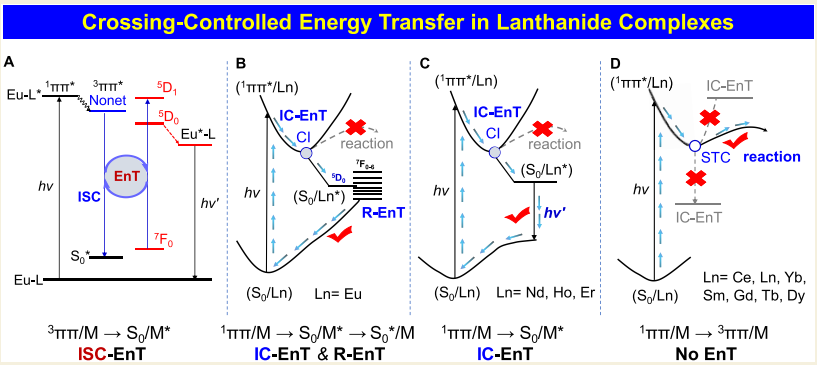

ABSTRACT: The structural, photophysical, and photochemical properties of Ln(depma)(hmpa)$_2$(NO$_3$)$_3$ (Ln = La, Ce, Nd, Sm, Eu, Tb, Ho, Er, and Yb) complexes **1-Ln** were investigated with a multidisciplinary approach involving synthesis, photocycloaddition-based crystal engineering, spectroscopic analytical techniques and quantum chemical ab initio calculations. Depending on the Ln^{3+} ion the isostructural **1-Ln** complexes exhibit quite different behavior upon excitation at 350−400 nm. Some **1-Ln** complexes (Ln = La, Ce, Sm, Tb, Yb) emit a broad and strong band near 533 nm arising from paired anthracene moieties, whereas others (Ln = Nd, Eu, Ho, Er) do not. **1-Eu** is not emissive at all, whereas **1-Nd**, **1-Ho**, and **1-Er** exhibit a Ln^{3+} based luminescence. Upon irradiation with 365 nm ultraviolet (UV) light **1-Ln** (Ln = La, Ce, Sm, Tb, Yb) dimerize by means of a photochemically induced [4 + 4] cycloaddition of the anthracene moieties, whereas **1-Ln** (Ln = Nd, Eu, Ho, Er) remain monomers. We propose three models, based on the matching of the energy levels between the Ln^{3+} ion and the paired or dimerized anthracene units in the energy-resonance crossing region, as well as on internal conversion-driven and intersystem crossing-driven energy transfer, which explain the Ln^{3+} ion regulated photophysics and photochemistry of the **1-Ln** complexes.

KEYWORDS: *lanthanide, anthracene, energy transfer, photophysics and photochemistry, photocycloaddition reaction, mechanism, ab initio calculations*

The anthracene photocycloaddition reaction is one of the oldest known photochemical reactions.[1] According to Schmidt, a prerequisite for anthracene [4 + 4] photodimerization to occur is that two anthracene rings must be face-to-face $\pi-\pi$ stacked with a spacing of less than 4.2 Å.[2] Early work has shown that under ultraviolet (UV) light irradiation the two stacked anthracene rings first form the excimer, where one anthracene in the excited singlet state is $\pi-\pi$ interacted with another in the ground state. The excimer can then either fluoresce via a radiative transition or be converted to the dimer via a nonradiative transition.[3] Due to the reversible nature of this photochemical reaction, a large number of organic anthracene derivatives have been reported, many of which have been used to construct photoresponsive mechanical materials,[4] smart dynamic polymers,[5] molecular sensors and devices.[6] In contrast, metal-anthracene complexes that have been reported to undergo photodimerization reactions are extremely rare.[7,8]

Lanthanide complexes have long been of interest because of their unique luminescent properties, such as long-lived excited states, low autofluorescence backgrounds, high penetration depths, and narrow-lined and characteristic emission covering

Received: June 24, 2024
Revised: August 24, 2024
Accepted: August 27, 2024
Published: September 9, 2024

the ultraviolet (UV), visible (vis) and near-infrared (NIR) ranges.[9] We envision that the construction of lanthanide−anthracene complexes will not only enrich the optical properties of anthracene-based compounds, but also lead to new responsive materials with intriguing functions. However, the photophysical processes of lanthanide complexes can be highly complicated since there are multiple competitive channels for excited state decay, including nonradiative relaxations with ligand-to-metal energy transfer (EnT), photodimerization and vibrational deexcitation, as well as emissions from ligand-centered fluorescence, and metal-centered luminescence. Moreover, additional radiative channels were also identified to be the EnT associated emissions from the excited states with the mixed spin.[10] As a result, the question arises as to how different lanthanide ions affect the photochemical and photophysical properties of lanthanide−anthracene complexes? To our surprise, a systematic study of the effect of lanthanide ion on anthracene photodimerization has never been documented.[11]

Lanthanide−anthracene complexes showcase complicated photophysical processes with multiple decay pathways. The transfer of energy from ligands to metals (EnT) plays a crucial role in switching between photochemical and photophysical routes. Sensitized intramolecular EnT, utilizing organic antennas as photosensitizers, effectively transfers light energy to lanthanide ions.[12] The f−f luminescence at the metal center in lanthanide complexes, governed by spin−orbit coupling (SOC) and magnetic dipole selection rules, has been extensively studied for over 80 years.[12b,c,13] However, the widely employed Förster and Dexter mechanisms,[12b,c,14] based on distance-dependent interactions, face challenges due to conflicting observations. Numerous complexes incorporating organic ligands exhibit strong luminescence despite unfavorable Förster or Dexter parameters.[12d,15] This is attributed to the limited spectral overlap between donor emission and lanthanide ion absorption. Alternative models such as inductive-resonant theory[16] and ligand-to-metal charge-transfer excitation[17] challenge traditional Förster or Dexter theories. A novel EnT model controlled by energy-degeneracy-crossing,[10] verified in europium complexes via quantum chemical calculations and experiments, offers insights without relying on Förster or Dexter parameters. In europium complexes, EnT regulation primarily involves ligand-centered SOC rather than distance-dependent factors. However, the applicability of this model to EnT events in other lanthanide complexes, especially those involving combined photophysical decay and photochemical reactions like lanthanide−anthracene complexes, remains uncertain. The photocycloaddition reaction and luminescent properties in lanthanide−anthracene systems are specific to the chosen lanthanide ion. A comprehensive understanding of the quantum correlations between lanthanide-centered luminescence and anthracene photocycloaddition is crucial for advancing anthracene-based photoresponsive lanthanide materials.

In this work, we report a series of mononuclear complexes, namely, $Ln(depma)(hmpa)_2(NO_3)_3$ (**1-Ln**, Ln = La^{3+}, Ce^{3+}, Nd^{3+}, Sm^{3+}, Eu^{3+}, Tb^{3+}, Ho^{3+}, Er^{3+}, and Yb^{3+}; depma = 9-diethylphosphonomethylanthracene, hmpa = hexamethylphosphoramide), which have the same structures as the Gd and Dy analogues. This series of complexes was chosen because our previous work has shown that under UV irradiation, Gd and Dy complexes can undergo an almost complete photocycloaddition reactions in a single-crystal-to-single-crystal (SCSC) fashion.[7a] Interestingly, the photophysical and photochemical properties of **1-Ln** are quite different. Compound **1-Ln** (Ln = La, Ce, Sm, Gd, Tb, Dy, Yb) emits yellow-green excimer fluorescence and undergoes a photocycloaddition reaction to form the binuclear compound $Ln_2(depma_2)(hmpa)_4(NO_3)_6$ (**2-Ln**). In contrast, the compounds **1-Nd**, **1-Ho**, and **1-Er** neither emit excimer emission nor undergo photocycloaddition reaction. Instead, they display NIR emission characteristic of the corresponding Ln^{3+} ions. **1-Eu** is the most unusual case, as it emits neither excimer emission nor the characteristic luminescence of the Eu^{3+} ion and does not undergo photocycloaddition reaction. Another interesting case is compound **1-Yb** which emits both excimer and NIR luminescence, and undergo photocycloaddition reaction. In order to understand the photophysical and photochemical processes triggered by light exposure of different **1-Ln**, we have performed quantum chemical calculations with the isomorphic complexes **1-Eu**, **1-Tb**, and **1-Ho** as representatives. By delving into the mechanism of ligand-to-metal energy transfer (EnT) and its function as a regulatory switch, we seek to manage the equilibrium between radiative and nonradiative pathways. Detailed exploration of mechanisms and kinetic analyses will assist in identifying modifiable parameters governing these processes.

EXPERIMENTAL AND COMPUTATIONAL DETAILS

General Information on Materials and Measurements

The syntheses of the compounds **1-Ln** and **2-Ln** were based on the previously reported methods.[7a] All other starting materials were of analytical grade obtained from commercial sources and used without any purification. A Perkin-Elmer 240C analyzer was used to do the elemental analyses for C, H, and N. Powder X-ray diffraction (PXRD) data were collected using a Bruker advance D8 diffractometer using Cu Kα radiation in a range of 5−50°. The Fourier infrared spectra were attained from a Bruker Tensor 27 spectrometer in the 4000−600 cm^{-1} region. The UV/vis spectra were measured on a Perkin-Elmer Lambda 950 UV/vis/NIR spectrometer using powder samples.

X-ray Crystallography

Single crystals were used for data collections on APEX II or APEX duo using graphite-monochromated Mo Kα radiation (λ = 0.71073 Å). The data were integrated using the Siemens SAINT program,[18] with the intensities corrected with a Lorentz factor as well as for polarization, air absorption, and absorption due to variation in the path length through the detector faceplate. Empirical absorption corrections were applied using the SADABS program.[19] The structures were solved by a direct method and refined on F^2 by full-matrix least-squares fitting using SHELXTL.[20] All the non-hydrogen atoms were refined anisotropically. All hydrogen atoms were located in a difference map, added geometrically, and isotropically refined with a riding model. The residual electron densities were of no chemical significance. CCDC 2233109−2233122 contain the supplementary crystallographic data for this paper. These data can be obtained free of charge from the Cambridge Crystallographic Data Centre via www.ccdc.cam.ac.uk/data_request/cif.

Luminescence Measurements

The steady fluorescence spectra were attained with a Perkin-Elmer Spectrofluorometer LS55. The time-resolved emission decay monitored at 533 nm and the absolute quantum yield of photoluminescence excited at 375 nm were measured on a Fluorolog-3 spectrofluorometer (Horiba Scientific) equipped with an integrating sphere. Nanosecond lifetime decays were conducted using a TCSPC MCA model equipped with a picosecond photodetector (<200 ps) (PPD850) and a picosecond laser (duration is 180 ps, Deltadiode, 100 MHz laser).

https://doi.org/10.1021/jacsau.4c00540
JACS Au 2024, 4, 3606−3618

Table 1. Selected Structural and Photophysical Parameters of 1-Ln and 2-Ln[a]

compound	**1-La**	**2-La**	**1-Ce**	**2-Ce**	**1-Nd**	**1-Sm**	**2-Sm**
space group	$P\bar{1}$	$P\bar{1}$	$P\bar{1}$	$P\bar{1}$	$P\bar{1}$	$P\bar{1}$	$P\bar{1}$
a (Å)	11.162(1)	11.078(6)	11.163(1)	11.072(3)	11.139(10)	11.149(1)	10.964(2)
b (Å)	11.446(1)	11.106(6)	11.349(1)	11.128(3)	11.306(10)	11.206(1)	11.037(2)
c (Å)	20.989(2)	21.191(12)	20.928(1)	21.207(6)	20.871(19)	20.812(2)	21.037(4)
α (deg)	78.718(1)	78.101(9)	79.245(1)	78.089(3)	79.911(16)	80.347(2)	88.129(2)
β (deg)	86.177(2)	87.525(9)	86.308(1)	87.458(3)	86.242(14)	86.479(2)	78.745(2)
γ (deg)	61.762(1)	62.848(9)	62.291(1)	62.944(3)	62.765(14)	63.626(2)	63.256(2)
V (Å^3)	2315.8(3)	2266(2)	2305.4(2)	2273.1(11)	2301(4)	2296.2(4)	2225.3(7)
Ln−O (Å)	2.397−2.635	2.393−2.645	2.381−2.638	2.382−2.625	2.344−2.601	2.319−2.570	2.270−2.541
O−Ln−O (deg)	47.5−156.8	47.8−158.4	48.2−156.8	48.3−158.0	49.0−155.9	49.6−154.2	49.8−155.9
d_{pp}	3.473		3.448		3.449	3.448	
d_{cc}	3.800		3.786		3.788	3.790	
$d_{C_6-C_{13}}$	3.761	1.66(1)	3.751	1.67(2)	3.778	3.759	1.66(1)
λ_{em} (nm)	533		533		870/1060	533	
τ (ns)	55(2)		34.8(1)			14.3(1)	
QY (%)	37(2)		15(2)			6 (1)	
compound	**1-Eu**	**1-Tb**	**2-Tb**	**1-Ho**	**1-Er**	**1-Yb**	**2-Yb**
space group	$P\bar{1}$	$P\bar{1}$	$P\bar{1}$	$P\bar{1}$	$P\bar{1}$	$P\bar{1}$	$P\bar{1}$
a (Å)	11.136(4)	11.0879(6)	10.965(1)	11.062(3)	11.104(4)	11.0278(6)	10.9295(19)
b (Å)	11.180(4)	11.1120(6)	11.066 (1)	11.090(3)	11.113(4)	11.0883(6)	11.0630(19)
c (Å)	20.742(7)	20.643(1)	21.021(2)	20.670(6)	20.638(3)	20.584(1)	20.990(4)
α (deg)	80.439(4)	86.517(1)	88.241(2)	86.680(4)	86.574(2)	86.516(1)	88.448(2)
β (deg)	86.449(4)	81.329(1)	78.976(2)	81.034(4)	81.299(2)	81.674(1)	79.213(2)
γ (deg)	63.754(4)	64.651(1)	63.361(2)	64.549(4)	64.572(2)	65.276(1)	63.570(2)
V (Å^3)	2283.8	2272.2(2)	2233.5(4)	2261.6(12)	2273.4(5)	2262.1(2)	2227.9(7)
Ln−O (Å)	2.303−2.565	2.250−2.540	2.270−2.541	2.245−2.542	2.235−2.548	2.214−2.551	2.236−2.546
O−Ln−O (deg)	49.9−153.6	50.8−152.4	50.1−154.6	50.9−152.4	50.1−152.6	51.5−150.1	50.3−152.9
d_{pp}	3.428	3.430		3.407	3.428	3.432	
d_{cc}	3.770	3.768		3.732	3.761	3.768	
$d_{C_6-C_{13}}$	3.745	3.743	1.699(7)	3.707	3.734	3.745	1.70(1)
λ_{em} (nm)		533		970	1530	533	
τ (ns)		70.6(2)				103.5(2)	
QY (%)		38(2)				72(2)	

[a] d_{pp}: interplanar distance, d_{cc}: center-center distance, d_{C6-C13}: the central C_6-C_{13} distance between the paired anthracene groups, τ: lifetime, QY: quantum yield.

Preparation of $Ln^{III}(depma)(hmpa)_2(NO_3)_3$ (1-Ln)

A mixture of 0.1 mmol $Ln(NO_3)_3{\cdot}6H_2O$, 0.1 mmol depma and 0.2 mmol hmpa in 5 mL CH_3OH was stirred at room temperature for half an hour. The resulted solution was filtered and left at room temperature for several days to yield yellow block crystals.

Preparation of $Ln_2(depma_2)(hmpa)_4(NO_3)_6$ (2-Ln)

Twenty mg of compound **1-Ln** (Ln = La, Ce, Sm, Tb, Yb) was irradiated under 365 nm UV light (ca. 100 mW/cm^2) for 5 h to afford **2-Ln** confirmed by PXRD and Fourier-transform infrared (FTIR) spectra.

Computational Details

Throughout the manuscript and the Supporting Information, the electronic states of the complexes are given as $^{2S+1}(R,M)_n$, where $2S + 1$ is the total spin multiplicity of the complex, R and M stand for the labels of the ligand and the Ln^{3+} ion (Ln = Eu, Tb, Ho), and n corresponds to the numbering of the electronic states $^{2S+1}(R,M)$ starting from $n = 0$ for the lowest state. It is important to distinguish this numbering of the electronic states of the complexes from the J levels of the Ln^{3+} central ion, although they sometimes take the same values, e.g., the ground state of the **1-Eu** complex is denoted as $^7(S_0/^7F_0)_0$. Omitting spin−orbit coupling the weak asymmetric ligand field splits $^7(S_0/^7F)$ into seven substates $^7(S_0/^7F)_n$ ($n = 0-6$). Using the state interaction approach, matrix elements over the spin−orbit Hamiltonian $\hat{H}_{SO}$ are computed based on these substates and the Hamiltonian matrix is diagonalized resulting in a total of $(2S + 1) \times (2L + 1) = 49$ energy levels. Including spin−orbit coupling Eu^{3+} $4f^6$ ^7F is split into seven levels ^7F_J ($J = 0-6$). The corresponding complex substates $^7(S_0/^7F_J)$ are again split due to the ligand field into $2J + 1$ levels each, yielding again a total of 49 energy levels. Since in the case of the Eu^{3+} complexes considered here spin−orbit interaction is stronger than the ligand field, one may keep the J value as a useful label for the $^7(S_0/^7F_J)_n$ ($J = 0-6$, $n = 0,1,...49$) energy levels of the complexes. By analogy, the electronic states can be labeled as $^7(S_0/^7F_J)_n$ ($J = 6-0$, $n = 0,1,...49$) for **1-Tb** and $^5(S_0/^5I_J)_n$ ($J = 8-4$, $n = 0,1,...65$) for **1-Ho**.

In this work, the ab initio calculations of the isolated anthracene dimer and the corresponding Eu(III), Tb(III), and Ho(III) complexes were primarily performed at the CASSCF level of theory with (8e/8o), (10e/11o), (12e/11o), and (14e/11o) active spaces, respectively. Based on the appropriate strategies of orbital localization and numerous computational tests, selection criteria were adopted to make use of a balanced model to describe the electron transitions in the specific chromophores of the ligands, and all configurations of six electrons in seven 4f orbitals for the Eu^{3+} center (6e/7o), eight electrons in seven 4f orbitals for the Tb^{3+} center (8e/7o), and ten electrons in seven 4f orbitals for the Ho^{3+} center (10e/7o). Energy-consistent scalar-relativistic Wood-Boring-adjusted 28-electron−core pseudopotentials were employed to account for the relativistic effects of Eu^{3+}, Tb^{3+}, and Ho^{3+} together with the corresponding basis sets.[21] C, O atoms were treated at the all-electron level with 6−31G* basis sets for central benzene rings of the anthracene and their substituent groups for free anthracene dimer and the **1-Ln** complexes while the C,

https://doi.org/10.1021/jacsau.4c00540
JACS Au 2024, 4, 3606−3618

H, O, N, and P atoms of the remaining moieties were calculated by using smaller basis sets (STO-3G for C, H, O, N, and STO-3G* for P) to reduce the computational burden (Figure S11). All minima of the free antennas and **1-Ln** complexes in their singlet excited states (S_{pp} and $^1\pi\pi^*$/M) were obtained by full-system state-averaged CASSCF optimizations using a two-root equally weighted approach. Whereas, a single-root optimization was adopted for ground (S_0 and S_0/M) and triplet states (T_{pp} and $^3\pi\pi^*$/M), together with the metal-centered quintet state ($S_0/^5D$) in **1-Eu** and **1-Tb**, and ($S_0/^5F$) in **1-Ho**. The minimum energy profiles for the photophysical and photochemical processes for the free anthracene dimer and the **1-Ln** complexes were mapped by intrinsic reaction coordinate (IRC) computations to connect the above critical points. To consider the dynamic electron correlation effects, single-point energies were evaluated at the CASPT2 level of theory based on the optimized structures of the IRC/CASSCF computations. All CASSCF calculations, together with the IRC pathway for the isolated anthracene dimer were performed using the Gaussian 03 program package.[22] The CASPT2 and SO calculations for the free ligands and all computations for the **1-Ln** complexes were carried out with the Molcas8.0 program package.[23]

RESULTS AND DISCUSSION

Crystal Structures of 1-Ln

Complexes **1-Ln** (Ln = La, Ce, Nd, Sm, Eu, Tb, Ho, Er, and Yb) were obtained as yellow crystals through the evaporation of a methanol solution containing $Ln(NO_3)_3$, depma, and hmpa in a 1:1:2 molar ratio. The structural parameters of **1-Ln** are summarized in Tables 1 and S1−S3, demonstrating that all compounds share isostructural architectures and crystallize in the triclinic system space group $P\bar{1}$. Each complex consists of one Ln^{3+}, one depma, two hmpa and three NO_3^-. The Ln^{3+} ion is coordinated by nine oxygen atoms, of which one is from depma, two are from hmpa and six are from three chelated nitrate anions (Figures 1 and S1). Due to the contraction effect of the lanthanides, the Ln−O bond lengths and O−Ln−O angles are slightly different, with the Ln−O bond lengths decreasing from the light lanthanide ion to the heavy lanthanide ion (Table 1). The most significant feature of the **1-Ln** structure is that the face-to-face $\pi-\pi$ stacking of the anthracene rings produces robust supramolecular dimers

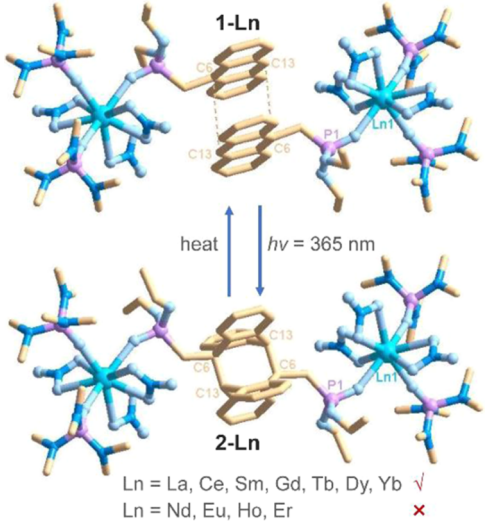

Figure 1. Reversible SCSC structural transformation between **1-Ln** (top) and **2-Ln** (bottom) (Ln = La, Ce, Sm, Gd, Tb, Dy, Yb) upon 365 nm irradiation and thermal annealing.

(interplanar distance d_{pp} = 3.407−3.473 Å, center-center distance d_{cc} = 3.732−3.800 Å), and the interactions between supramolecular dimers are governed by van der Waals forces. Despite minor fluctuations in bond parameters, the complexes exhibit similar cell volumes ranging from 2315.8 to 2261.6 Å^3. These crystal parameters imply that the structural variations induced by different Ln^{3+} ions are negligible and improbable to explain the observed discrepancies in photochemical and photophysical properties.

Photophysical Properties of 1-Ln

UV−vis diffuse reflectance spectroscopy was employed to analyze the absorption properties of the **1-Ln** complexes. The spectra unveiled robust absorption bands within the 300−450 nm range for all **1-Ln** complexes, peaking at 380−400 nm (Figure S2). To provide a clear assignment of the antenna absorption in the diffuse reflectance spectroscopy, the vertical excited properties for anthracene monomer and dimer were first computed (Table S9). The results reveal that the highest occupied molecular orbital (HOMO) → lowest-unoccupied molecular orbital (LUMO) transition of anthracene monomer features a $\pi-\pi^*$ excitation with a moderate oscillator strength (f = 0.187). However, for anthracene dimer, i.e., in the presence of the second anthracene, the oscillator strength of this bright state significantly increased (f = 0.928), accompanied by a slight redshift in absorption to λ_{abs} = 369 nm. This augmentation is ascribed to strong quantum coupling between the bright states of the two anthracene moieties, elucidating why the anthracene dimer functions as an optimal antenna ligand for sensitized energy transfer in Ln complexes. Moreover, a relatively feeble $\pi-\pi^*$ excited state at λ_{abs} = 295 nm with a low oscillator strength (f = 0.069) was observed, corresponding to the experimentally measured shoulder band near 280 nm in the diffuse reflectance spectra of the Ln complexes. Additionally, the spectra exhibited distinctive peaks attributed to f−f transitions of the Ln^{3+} ions. For instance, **1-Sm** manifested transitions at 465 and 478 nm ($^6H_{5/2} \rightarrow {}^4I_{13/2}$, $^6H_{5/2} \rightarrow {}^4I_{11/2}$), **1-Eu** exhibited transitions at 466 and 536 nm ($^7F_1 \rightarrow {}^5D_1$, $^7F_0 \rightarrow {}^5D_2$), and **1-Tb** displayed a transition at 488 nm ($^7F_6 \rightarrow {}^5D_4$).[24] These f−f transitions were more prominent in **1-Ln** complexes with **Ln** = Nd, Ho, and Er. Specifically, **1-Ho** showcased four distinct absorption peaks at 454, 484, 539, and 645 nm, corresponding to $^5I_8 \rightarrow {}^5G_6$, $^5I_8 \rightarrow {}^5F_3$, $^5I_8 \rightarrow {}^5F_4$, and $^5I_8 \rightarrow {}^5F_5$ transitions, respectively (Table S4).

Upon excitation within the 350−400 nm range, specific **1-Ln** complexes (Ln = La, Ce, Sm, Gd, Tb, Dy, and Yb) showcased a robust and wide emission band peaking around 533 nm, stemming from the excimer emission of face-to-face paired anthracene groups (Figures 2 and S3).[25] This emission pattern corresponds to theoretical calculations predicting an emission at 544 nm for the anthracene excimer (Figure 3). For instance, **1-Tb** exhibited a lifetime of 70.6 ns at 533 nm and a quantum yield of 38.0% excited at 375 nm (Tables 1 and S5). However, the unique excimer emission was not observed for **1-Eu** (Figure 2E), despite its isostructural nature with other **1-Ln** complexes. Similarly, excimer emission was not detected for **1-Nd**, **1-Ho**, and **1-Er**. Instead, narrowed emission peaks appeared at 870/1060 nm (Nd^{3+}), 970 nm (Ho^{3+}), and 1530 nm (Er^{3+}) upon photoexcitation at 380 nm, corresponding to the Nd^{3+}: $^4F_{3/2} \rightarrow {}^4I_{9/2}/{}^4F_{3/2} \rightarrow {}^4I_{11/2}$, Ho^{3+}: $^5F_5 \rightarrow {}^5I_7$, and Er^{3+}: $^4I_{13/2} \rightarrow {}^4I_{15/2}$ transitions, respectively (Figures 2C,G,H and S4−S6). In particular, **1-Yb** exhibit excimer

https://doi.org/10.1021/jacsau.4c00540
JACS Au 2024, 4, 3606−3618

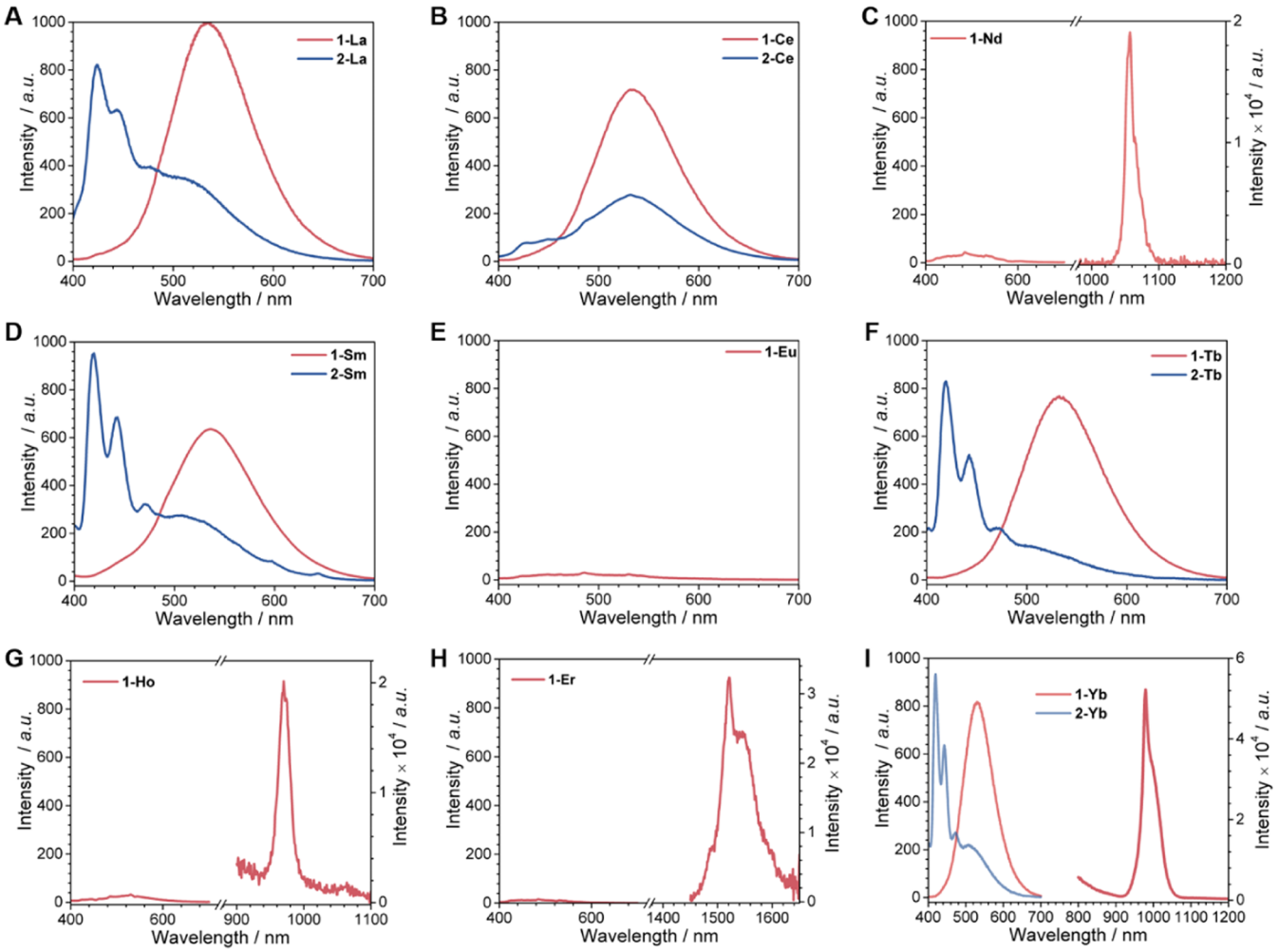

Figure 2. Emission spectra for all **1-Ln** (Ln = La (A), Ce (B), Sm (D), Eu (E), and Tb (F)) excited at 375 nm and **2-Ln** excited at 371 nm. The NIR emission spectra for **1-Nd** (C), **1-Ho** (G), **1-Er** (H), and **1-Yb** (I) are excited at 380 nm.

emission near 533 nm and NIR emission peaking at 980 nm due to the $^2F_{5/2} \rightarrow {}^2F_{7/2}$ transition of Yb^{3+} ion (Figures 1 and S7). These results indicate that the anthracene group is not effective in sensitizing the emission of Ce^{3+}, Sm^{3+}, Gd^{3+}, Tb^{3+}, and Dy^{3+} ions due to an energy mismatch.[26] However, it efficiently sensitizes the near-infrared (NIR) emission of Nd^{3+}, Ho^{3+}, Er^{3+}, and Yb^{3+} ions, which possess excited states at lower energies than anthracene (approximately 670 nm).[26,27] The fact that **1-Yb** emits both excimer and NIR luminescence suggests that the energy transfer from anthracene to Yb^{3+} ion is incomplete. Nevertheless, the behavior of **1-Eu** remains ambiguous and puzzling, as it does not conform to this mechanism.

Photochemical Reactions of 1-Ln

The results highlighted above underscore the significant dependence of the photophysical properties of **1-Ln** on the specific lanthanide ion. To explore the photocycloaddition reactions, crystals of **1-Ln** were exposed to 365 nm UV light and the resulting products were analyzed using techniques such as single-crystal structural analysis, powder X-ray diffraction (PXRD), infrared (IR) spectroscopy, UV−vis diffuse reflectance, and photoluminescence (PL) spectroscopy. Structural analyses confirmed that **1-Ln** (Ln = La, Ce, Sm, Tb, and Yb), akin to **1-Gd** and **1-Dy**, underwent a photodimerization reaction, leading to the formation of $Ln_2(depma_2)(hmpa)_4(NO_3)_6$ (**2-Ln**) (Tables S6 and S7 and Figure S8). In contrast, **1-Nd**, **1-Eu**, **1-Ho**, and **1-Er** remained unchanged upon UV light irradiation, as supported by PXRD and IR spectra (Figures S9 and S10).

Given that the **2-Ln** compounds share an identical structure, we've opted to use **2-Tb** as a representative for structural depiction. **2-Tb** crystallizes in the triclinic system, space group $P\bar{1}$. It embodies a binuclear structure where the equivalent $Tb(hmpa)_2(NO_3)_3$ units link through a photodimerized anthracene ($depma_2$) bridge (Figure 1). Within $depma_2$, the central C6−C13′ distance measures 1.699(7) Å, significantly shorter than that in **1-Tb** (3.743 Å). The formation of C−C single bonds between the central benzene rings of the two anthracene moieties in **2-Tb** reduces the conjugation of the anthracene skeleton, which manifests in altered photophysical properties. In comparison to the diffuse reflectance spectrum of **1-Tb**, the intensity of the broad absorption band at 398 nm diminishes in **2-Tb**, displaying emerging vibronic structures (Figure S2). Moreover, the intensity of the absorption peak at 280 nm considerably increases. Substantial alterations are observed in the photoluminescent properties before and after the photocycloaddition reaction. The intensity of the excimer emission peak at 533 nm in **1-Tb** notably diminishes in **2-Tb**, replaced by structural peaks at 400, 424, 446, and 475 nm (Figure 2), attributable to the $\pi-\pi^*$ transition of the

https://doi.org/10.1021/jacsau.4c00540
JACS Au 2024, 4, 3606−3618

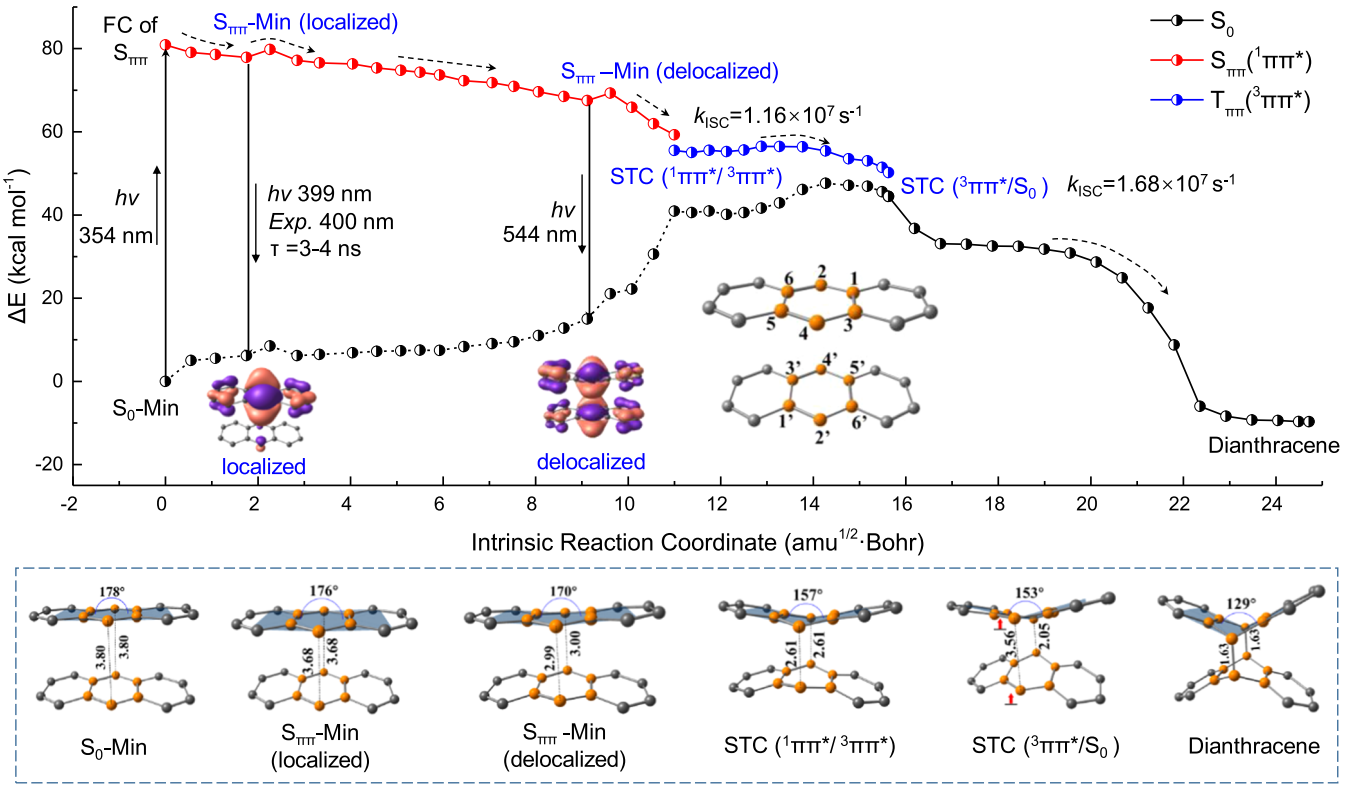

Figure 3. Minimum energy profiles (MEPs) of the stepwise mechanism are shown for the [4 + 4] photodimerization of free anthracene dimer calculated at the CASPT2//IRC//CASSCF(8e/8o) level of theory. The numbering of the central benzene rings (highlighted in orange) of the anthracene is inserted in the right panel. Schematic structures for critical points along the [4 + 4] photodimerization path are given in the lowest panel together with the bond lengths (distances) in Å.

dianthracene moiety.[7] Comparable structural and optical spectral changes were observed for **1-La**, **1-Ce**, **1-Sm**, and **1-Yb** (Figures 1 and 2). However, the UV−vis diffuse reflectance and PL spectra of 1-Nd, 1-Eu, 1-Ho, and 1-Er remain unaltered after UV light irradiation.

Quantum Chemical Calculations

The experimental findings gathered for **1-Ln** unequivocally demonstrate that the photophysical and photochemical characteristics of lanthanide−anthracene complexes are markedly impacted by the specific lanthanide ion incorporated. To delve deeper into comprehending the underlying mechanism dictating the diverse behavior of these complexes, minimum energy profiles (MEPs) were calculated for photophysical and photochemical relaxations. These calculations encompassed not only the free anthracene dimer (Figure 3), but also **1-Eu**, **1-Ho**, and **1-Tb** as representatives (Figures 4, 5, and 6). The computational approach employed entailed a multiconfigurational quantum chemical method (CASSCF/CASPT2) in conjunction with relativistic energy-adjusted ab initio Ln pseudopotentials. This computational methodology facilitates a more precise and comprehensive exploration of the electronic structure and dynamic behaviors within the lanthanide−anthracene complexes.

We commenced our investigation by scrutinizing photophysical and photochemical process of the isolated anthracene dimer, denoted as **AA**. Upon experimental photoexcitation at a wavelength of 365 nm, **AA** is promoted to the Franck−Condon (FC) region of a bright state ($^1\pi\pi^*$), labeled as $S_{\pi\pi}$. This state originates from a localized excimer excitation (**A***A), involving quantum coupling between one ring exhibiting a $\pi-\pi$ excitation (**A***) and another ring in the ground state (**A**). The vertical excitation energies for the $S_0 \rightarrow S_{\pi\pi}$ transition for **AA** and its Ln complexes (Ln = Eu, Tb, and Ho) were theoretically calculated within the range of 77.4 to 80.9 kcal mol^{-1} (354−369 nm, Table S8). These calculations confirm the stability of energy levels and optical properties across different chemical environments.

Following the FC excitation, the **A***A state rapidly undergoes decay to reach the minimum of $S_{\pi\pi}$, termed $S_{\pi\pi}$-Min, with an energy decrease of approximately ∼3 kcal mol^{-1}. In the excited **A** ring, there are slight structural adjustments observed in all C−C bonds, while their counterparts in the **A** ring remain nearly unchanged, signifying the nature of single **A** ring excitation. The theoretically predicted fluorescence emission for the $S_{\pi\pi}$-Min (localized) → S_0 transition occurs at 399 nm, consistent with the experimentally measured emission peak at 400 nm in methanol solution with a lifetime of 4 ns (Table S5).

The interaction between the rings is notably intensified by increased $\pi-\pi$ orbital coupling, evident in the reduced distances between the two **A** rings along the relaxation path in the $S_{\pi\pi}$ state. Through unrestricted CASSCF optimizations, we've identified another minimum at an inter-ring distance of 3.0 Å (equal distances of C2−C4′ and C4−C2′), representing a state characterized by delocalized excimer excitation within the energy plateau of the $S_{\pi\pi}$ state. In this state, the bridged benzene moieties (highlighted in orange) concurrently expand for the paired **A** rings. In contrast to the emission (399 nm) from $S_{\pi\pi}$-Min (localized), a red-shifted fluorescence emission at 544 nm is theoretically calculated for the delocalized excimer minimum, termed $S_{\pi\pi}$-Min (delocalized). This theoretical

https://doi.org/10.1021/jacsau.4c00540
JACS Au 2024, 4, 3606−3618

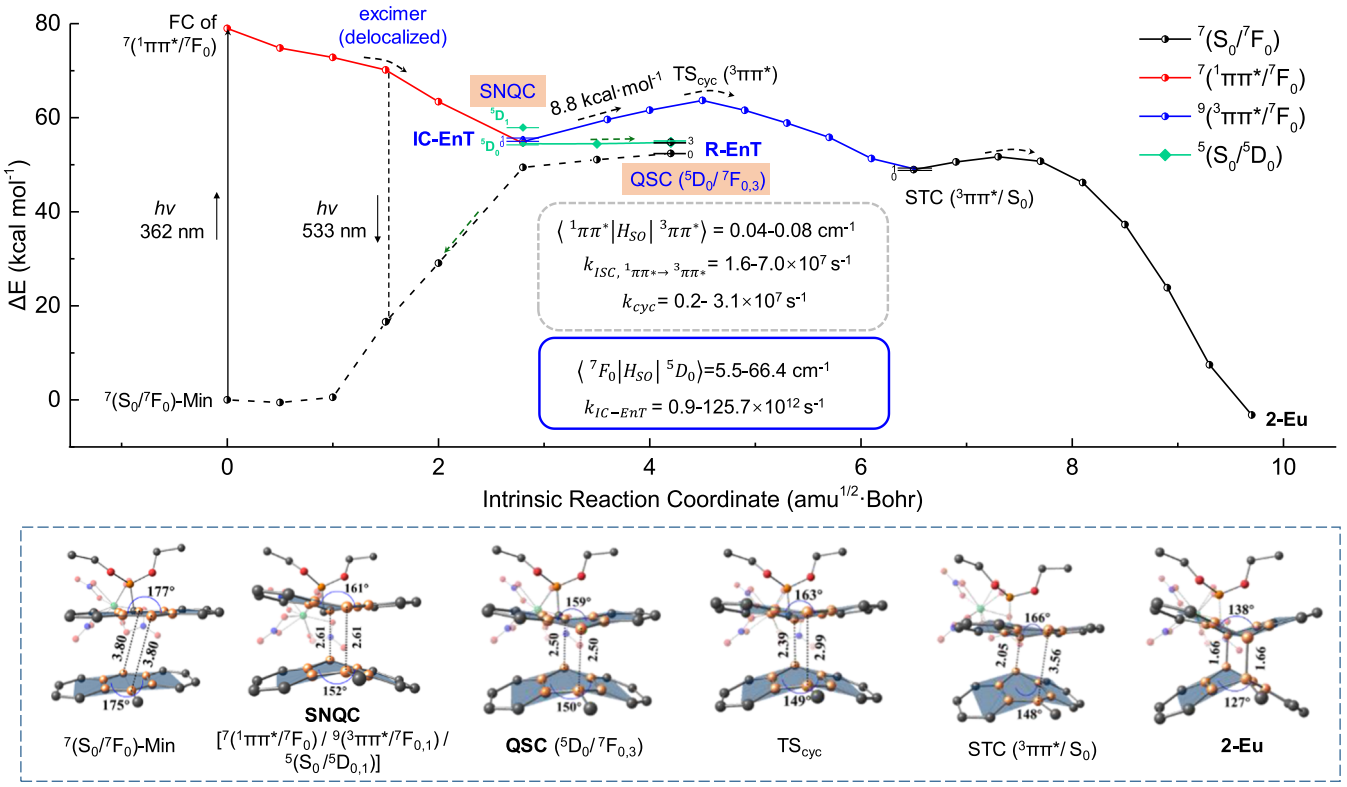

Figure 4. Excited state deactivation pathway for **1-Eu**. Minimum energy profiles (MEPs) for the photophysical and photochemical processes for **1-Eu** (neither emission nor reaction) calculated at the CASPT2//IRC//CASSCF(10e/11o) level of theory. The septet-nonet-quintet crossing (SNQC) represents the three-states crossing among septet $^7(^1\pi\pi^*/^7F_0)$, nonet $^9(^3\pi\pi^*/^7F_0)$, and quintet $^5(S_0/^5D_0)$ states. The emission is quenched by the reverse energy transfer [$^5(S_0/^5D_0) \rightarrow {}^7(S_0^*/^7F_3)$] (R-EnT). The quintet-septet crossing (QSC) represents the two-states crossing between quintet $^5(S_0/^5D_0)$ and septet $^7(S_0/^7F_3)$ states. IC-EnT is defined as the energy transfer driven by internal conversion (IC, $^1\pi\pi^* \rightarrow S_0$). Schematic structures for critical points along the [4 + 4] photodimerization and the energy transfer paths of **1-Eu** are provided in the lower panel along with characteristic interatomic distances in Å.

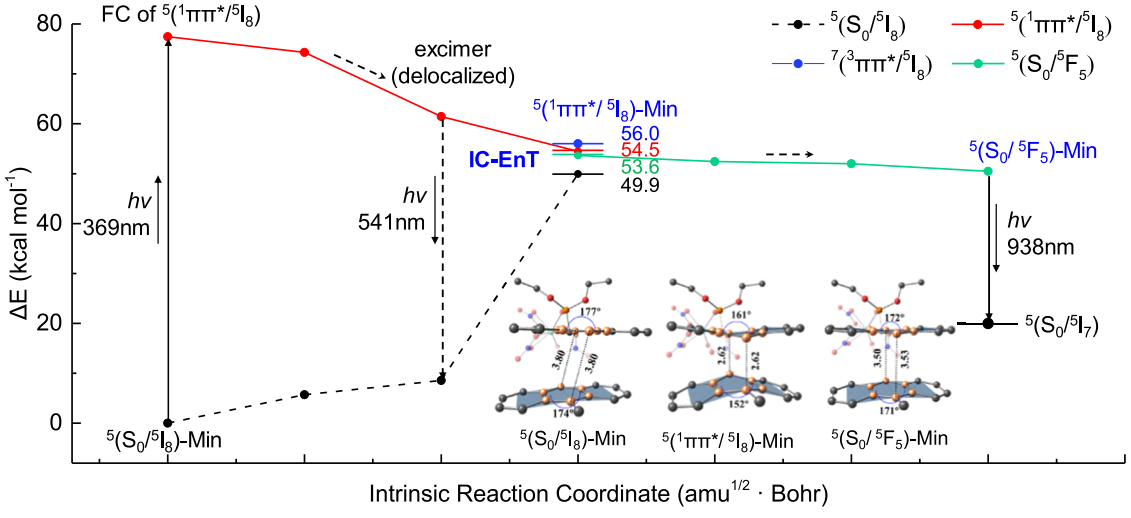

Figure 5. Excited state deactivation pathway for **1-Ho.** Minimum energy profiles (MEPs) for the photoluminescence decay of **1-Ho** complex calculated at the CASPT2//IRC//CASSCF(14e/11o) level of theory. Schematic structures for critical points along the radiative path of **1-Ho** are given in the lower panel together with the bond distances in Å.

calculation aligns well with experimental measurements (530–533 nm) observed in a series of **1-Ln** complexes upon 365 nm light irradiation (Ln = La, Ce, Sm, Gd, Tb, Dy, and Yb), except for **1-Ln** (Ln = Nd, Eu, Ho, and Er).

Notably, the predicted emission wavelength (544 nm) at a 3.0 Å inter-ring distance significantly exceeds the solid-state emission (426 nm). Through various test calculations, it is been established that the [4 + 4] photocycloaddition inevitably occurs when the inter-ring distance falls below 3.0 Å (refer to Figure S16). Hence, the $S_{\pi\pi}$-Min (delocalized) transition, with a 3.0 Å inter-ring distance, is considered as the critical structure for excimer emission, indicating the fluorescence emission

https://doi.org/10.1021/jacsau.4c00540
JACS Au 2024, 4, 3606–3618

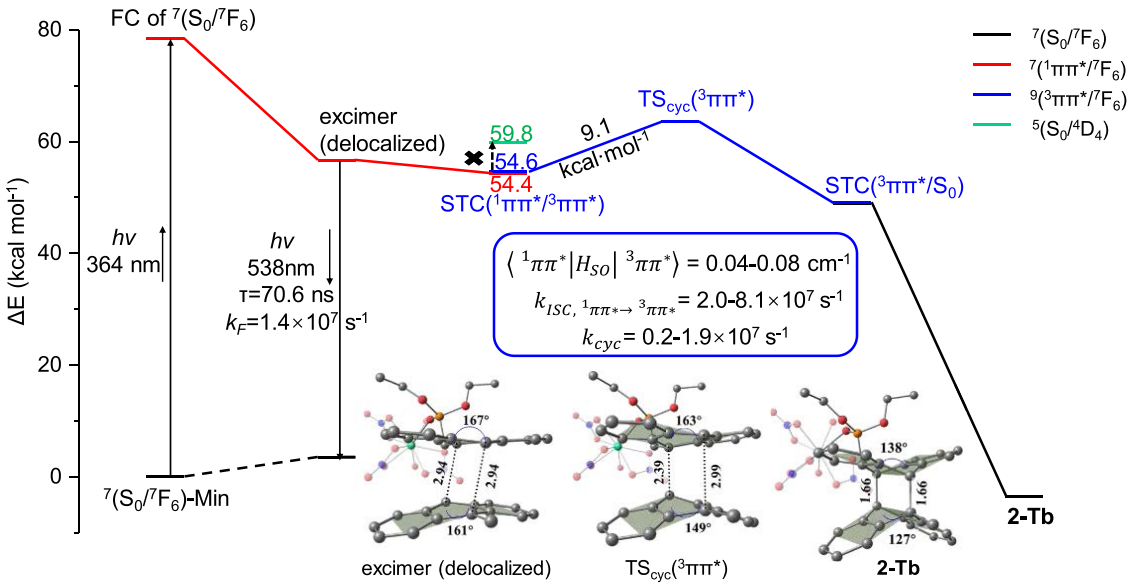

Figure 6. Excited state deactivation pathway for **1-Tb.** Minimum energy profiles (MEPs) for the stepwise [4 + 4] photodimerization and the excimer emission of **1-Tb** complex calculated at the CASPT2//IRC//CASSCF(12e/11o) level of theory. Schematic structures for critical points along the radiative path of **1-Tb** are given in the lower panel together with the bond distances in Å.

around 500 nm as an indicator of the [4 + 4] photocycloaddition reaction occurrence, particularly in a constrained crystal environment. Additionally, the combined theoretical and experimental evidence confirms the validity of Schmidt's rule.[2]

Once the excimer moves away from the $S_{\pi\pi}$-Min (delocalized) region by surpassing a small barrier (1.8 kcal mol^{-1}), it encounters a singlet−triplet crossing (STC) between the $S_{\pi\pi}(^1\pi\pi^*)$ and $T_{\pi\pi}(^3\pi\pi^*)$ states. This crossing happens at equidistant C2−C4′ and C4−C2′ distances of 2.61 Å, accompanied by a bending in the dihedral angles C1C2C4C6 and C1′C2′C4′C6′ from 170 to 157°. Despite a non-negligible energy gap (3.7 kcal mol^{-1}) and relatively weak spin−orbit coupling (SOC) (0.11 cm^{-1}) for the pure organic system, the intersystem crossing (ISC) from $S_{\pi\pi}$ to $T_{\pi\pi}$ occurs with moderate efficiency (k_{ISC1} = 1.16 × 10^7 s^{-1}). This brings the system to populate the $T_{\pi\pi}$ state with significant diradical character. Consequently, the concerted asynchronous C to C′ approach progresses, subsequently relaxing to a $T_{\pi\pi}/S_0$ STC at distances of 2.05 Å (C2−C4′) and 3.56 Å (C4−C2′). Similar to the earlier scenario, the ISC from $T_{\pi\pi}$ to S_0 occurs within the time scale of 10^{-7} s^{-1}, indicating that the photocycloaddition for isolated **A** is a minor channel ($\Phi_{cyclo,exp}$ = 0.1)[28] compared to the fluorescence emission ($\Phi_{em,\ exp}$ = 0.3−0.5). The final cycloaddition reaction occurs efficiently along a downhill path in the ground state, resulting in the production of the dianthracene product with 9.7 kcal mol^{-1} exothermicity.

Theoretical Models and Kinetic Evaluations

To establish a universal strategy governing the photophysical and photochemical behavior regulated by Ln^{3+}, the MEPs were mapped for three typical isomorphic lanthanide compounds: **1-Eu**, **1-Ho**, and **1-Tb**, shown in Figures 4−6, respectively. Concurrently, kinetic evaluations were performed to calculate EnT rates and photocycloaddition reaction rates, revealing pivotal factors in controlling the dynamic interplay between radiative and nonradiative channels. Upon 365 nm UV-light irradiation, the **1-Ln** complexes were swiftly promoted to the FC bright spectroscopic state, originating from the ligand-centered $\pi-\pi^*$ excitation (f = 0.28−0.50), concomitant with the Ln^{3+} in ground state configuration—$^7(^1\pi\pi^*/^7F_0)$, $^7(^1\pi\pi^*/^7F_6)$, and $^5(^1\pi\pi^*/^5I_8)$ for **1-Eu**, **1-Tb**, and **1-Ho**, respectively. Subsequently, the complexes rapidly decayed to an energy plateau, characterized by a delocalized excimer excitation. The distinct emission at ∼540 nm signified radiative decay from this plateau, engaging in dynamic competition with subsequent cycloaddition reactions and ligand-to-metal EnT. Multiple test calculations demonstrated that the initial decay of excited states for all investigated **1-Ln** complexes aligned well with the photophysical behaviors of an isolated **A** dimer (Figure S17). As the excited state decay of the complexes approached the ligand-centered $^3\pi\pi^*$ state, the precursor of the cycloaddition reaction, dynamic differences gradually emerged.

The minimum energy point of ligand-centered $^1\pi\pi^*$, denoted as $^7(^1\pi\pi^*/^7F_0)$-Min, for the **1-Eu** complex, is identified at equidistant positions of 2.61 Å for C2-C4′ and C4-C2′, exhibiting a significant energy decrease exceeding 20 kcal mol^{-1} in the decay from FC (Figure 4). Similar to the anthracene dimer scenario, at such a short inter-ring distance, the delocalized excimer excitation was characterized alongside the charge transfer between the two anthracenes (Figure S17). This inherent delocalization results in the $^1\pi\pi^*$ and $^3\pi\pi^*$ states tending to have similar energies. Additionally, due to the significant deformation of anthracenes, the energy of the ground state (S_0*) also increases significantly. Energy assessments at the CASPT2 level reveal the energetic equivalence of the $^1\pi\pi^*$ state with both the ligand-centered $^3\pi\pi^*$ state and the metal-centered excited $^5D_0$ state. Consequently, a three-state crossing, that is the septet $^7(^1\pi\pi^*/^7F_0)$, nonet $^9(^3\pi\pi^*/^7F_0)$, and quintet $^5(S_0/^5D_0)$ states (SNQC), emerges at an adiabatic energy level of approximately 55 kcal mol^{-1} (19200 cm^{-1}), relative to $^7(S_0/^7F_0)$-Min, closely aligning with the optimal ligand-centered triplet energy for ligand-to-metal EnT (approximately 20,000 cm^{-1}).[13] This SNQC acts as a dynamic gate for both EnT via a $^7(^1\pi\pi^*/^7F_0) \rightarrow {}^5(S_0/^5D_0)$ transition and the initiation of the cycloaddition reaction through a $^7(^1\pi\pi^*/^7F_0) \rightarrow {}^9(^3\pi\pi^*/^7F_0)$ transition.

https://doi.org/10.1021/jacsau.4c00540
JACS Au 2024, 4, 3606−3618

Scheme 1. Proposed Theoretical Models to Account for the Different Dynamic Behavior of Photophysical and Photochemical Processes of Ln^{3+} Complexes[a]

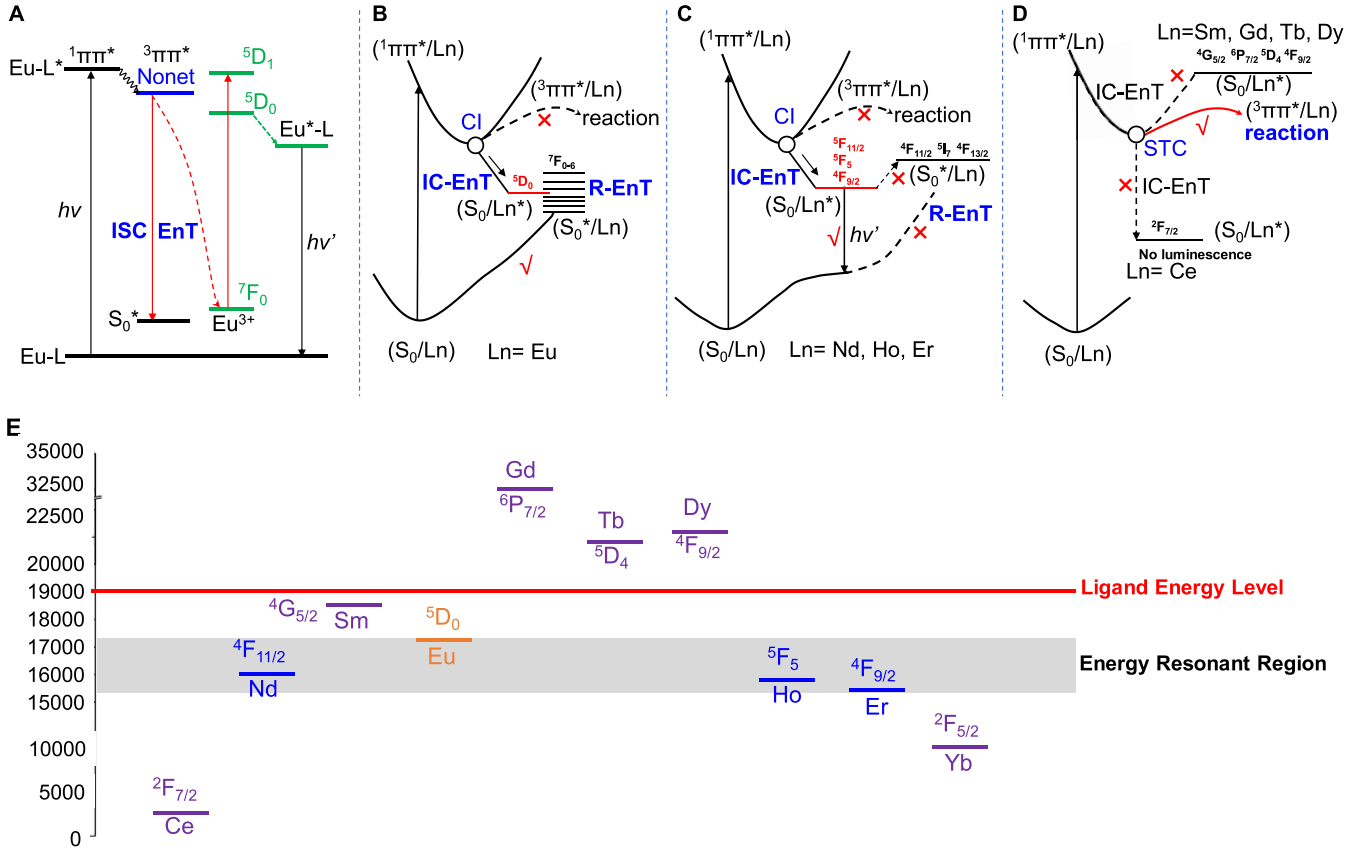

[a](A) The model of ISC-controlled ($^3\pi\pi^*$ → S_0) EnT (see ref 10). (B) The model of IC-driven ($^1\pi\pi^*$ → S_0) EnT with R-EnT: EnT can operate efficiently, but the metal-centered emission is quenched by the R-EnT (neither emission nor reaction). (C) The model of IC-driven ($^1\pi\pi^*$ → S_0) EnT without R-EnT (metal-centered emission). (D) The absence of energy-resonance crossing ([4 + 4] photocycloaddition reaction). (E) Energetic diagram for excited-state levels of different Ln^{3+} compared to those of ligand energy level and energy resonant region. Energy levels of lanthanide ions were obtained from ref 12b. The optimal energy transfer region for anthracene is highlighted in gray, which locates energetically 1750−3800 cm^{-1} below the anthracene-centered $^1\pi\pi^*$ singlet excited state (red line) in our IC-driven EnT model. The UV irradiated anthracene ligand can be used to differentiate Ln^{3+} into three categories: photoluminescence (Nd^{3+}, Ho^{3+}, and Er^{3+}), photocycloaddition (Ce^{3+}, Sm^{3+}, Gd^{3+}, Tb^{3+}, Dy^{3+}, and Yb^{3+}), and neither emissive nor reactive (Eu^{3+}), highlighted in blue, purple and orange, respectively. ISC, intersystem crossing; IC, internal conversion, STC, singlet-triplet crossing; CI, conical intersection.

Although the ISC (intersystem crossing) rates of the free **A** dimer and **1-Eu** occur at a similar time scale (10^7 s^{-1}), their respective cycloaddition processes differ significantly. The moderate barrier in the ligand-centered $^3\pi\pi^*$ state (TS_{cyc} ($^3\pi\pi^*$)) (ΔE = 8.8 kcal mol^{-1}, $\Delta G^{\ddagger}$ = 7.2 kcal mol^{-1}) for **1-Eu** along the cycloaddition pathway arises due to constrained anthracene ring deformations in the confined crystal environment. According to transition state theory (TST), the computed reaction rate is 3.1 × 10^7 s^{-1}, notably slower compared to the EnT process via the $^7(^1\pi\pi^*/^7F_0)$ → $^5(S_0/^5D_0)$ transition within 0.9−125.7 × 10^{12} s^{-1}. Consequently, the presence of this barrier moderately reduces the efficiency of the cycloaddition reaction, favoring EnT as the primary pathway for excited state decay in **1-Eu**.

As depicted in Figure 4 and Scheme 1, the EnT mechanism observed in the anthracene-coordinated Eu^{3+} complex markedly differs from that of Eu^{3+} complexes involving 1-hydroxypyridin-2-one (1,2-HOPO) and 1-phenyl-3-pyridin-3-yl-propane-1,3-dione (PPPD) ligands.[10] In the latter, the ligand-centered ISC $^3\pi\pi$ → S_0* transition facilitates the release of excitation energies, driving the metal-centered 4f electron pairing and consequently generating the emissive excited $^5D_0$ state (Scheme 1A). The significant discovery lies in the presence of a nonet-quintet crossing within the energetically sensitive resonance region. In the case of the anthracene complex, the emissive $^5D_0$ state aligns energetically with both the ligand-centered $^1\pi\pi^*$ and $^3\pi\pi^*$ states simultaneously. This introduces an alternative and more efficient EnT pathway that releases ligand-centered excitation energies through internal conversion (IC) $^1\pi\pi^*$ → S_0. The presence of a multistate crossing predominantly arises from the rapid elevation of the S_0 energy level due to extensive anthracene ring bending deformations. Notably, the energy level of S_0 achieves quasi-degeneracy with $^1\pi\pi^*$ and other excited states (such as ligand-centered $^3\pi\pi^*$ and metal-centered $^5D_0$) at the critical point of SNQC. This scenario allows for IC-driven EnT to prevail over ISC-controlled EnT within a nanosecond time scale.[10b]

Figure 5 illustrates CASPT2 results for Ho^{3+}, which consistently reveal multistate degenerate crossings involving the ligand-centered $^1\pi\pi^*$ and $^3\pi\pi^*$ states, along with the emitting state of Ln^{3+}. This occurrence is particularly notable in the anthracene-coordinated complexes of Ho^{3+}, Nd^{3+}, and

https://doi.org/10.1021/jacsau.4c00540
JACS Au 2024, 4, 3606−3618

Er^{3+}, where these energy-resonance crossings for ligand-to-metal EnT are situated at approximately 53.0−54.5 kcal mol^{-1} (about 19,000 cm^{-1}) relative to (S_0/Ln)-Min. Moreover, they are positioned 1750−3800 cm^{-1} higher than the emitting levels of the lanthanide ions (Eu^{3+}, Ho^{3+}, Nd^{3+}, and Er^{3+})[12b] in the absence of a ligand field. In the presence of coordinating ligands, the metal-centered emitting level experiences an inevitable blue shift (ranging from 1700−3500 cm^{-1}) and aligns energetically with the energy level of the ligand-centered singlet or triplet excited state. Hence, the key criterion for energy-matching controlled EnT lies in the optimal energy difference between the ligand-centered donor and the emitting level of the free lanthanide ion, ideally falling within a range of 1750 to 3800 cm^{-1} for anthracene-coordinated Ln^{3+} complexes.

Drawing from this selection rule based on resonant energy matching between the ligand and Ln^{3+}, four theoretical models are proposed and depicted in Scheme 1. These models aim to elucidate the dynamic gate-opening behavior between the radiative and nonradiative channels. First of all, the substantial structural deformation of the ligand markedly elevates the energy of the ligand-centered S_0 state, thereby increasing the number of involved excited states within the energy-resonance crossing region. Consequently, this potentially activates a more efficient channel for internal conversion (IC)-driven EnT (Scheme 1B,C), compared with the frequently utilized model of ISC-controlled EnT (Scheme 1A). Following the IC-driven EnT model and the energy-matching selection rule, only Eu^{3+}, Ho^{3+}, Nd^{3+}, and Er^{3+} coordinated anthracene complexes are anticipated to efficiently undergo ligand-to-metal EnT, exhibiting the suitable energy difference between the ligand-centered donor and the emitting level of the free lanthanide ion (Scheme 1E).

Second, upon the efficient completion of EnT, the $^5D_0/^7F_3$ crossing is encountered along the decay pathway of the **1-Eu** complex in the emissive $^5(S_0/^5D_0)$ state. This crossing allows for the occurrence of reverse EnT (R-EnT) through the transition of $^5(S_0/^5D_0) \rightarrow {}^7(S_0{}^*/^7F_3)$, resulting in a significant quenching in luminescence. This scenario primarily arises from the high density of states among the sublevels of the ground state of Eu^{3+} (^7F_J, J = 0−6) within a narrow energy range (approximately 5 kcal mol^{-1}) and the rapid increase in S_0 energy (ligand-centered) due to substantial structural deformation of the anthracene ring. We note here in passing that the lowering of the symmetry reduces the ^7F spin−orbit splitting by almost a factor of 3 compared to the free Eu^{3+} ion. The specific case concerning the relaxation of the emissive state in the **1-Eu** complex contributes to a nonradiative Internal Conversion (IC)-driven EnT model, as depicted in Scheme 1B. This model helps elucidate why neither excimer nor Eu^{3+} emissions are observed in the UV-irradiated **1-Eu** complex. According to our theory analysis provided in Section 5.2 of the SI, the energy associated with ligand-to-metal charge transfer (LMCT) is even higher than that of the double excitations ($^1\pi\pi^*/^5D_J$), suggesting that LMCT transitions would not be populated under the current conditions.[29] Excluding low-lying LMCT in **1-Eu** is further confirmed by the absence of new absorption bands above 500 nm for **1-Eu** in comparison to closed-shell **1-La** (Figure S2).

Third, compared to the **1-Ho**, **1-Nd**, and **1-Er** complexes, the electronic structure of the ligand-coordinated Eu^{3+} ion offers more opportunities for the emissive level ($S_0/^5D_0$) of the **1-Eu** complex to energetically align with the sublevels of the ground state ($S_0{}^*/^7F_J$). In contrast, for the aforementioned cases of **1-Ho**, **1-Nd**, and **1-Er**, no energetically accessible metal-centered ground state sublevels match the corresponding emissive level. For example, the energy gaps between the two lowest-lying levels are 5000 cm^{-1} for Ho^{3+} ($^5I_8-{}^5I_7$), 6500 cm^{-1} for Er^{3+} ($^4I_{15/2}-{}^4I_{13/2}$), and 2500 cm^{-1} for Nd^{3+} ($^4I_{9/2}-{}^4I_{11/2}$),[12b] respectively, positioning energetically above the relaxation path line of the emissive state. Consequently, the higher energy levels of ^5I_J (J = 7−4) for Ho^{3+}, ^4I_J (J = 13/2−9/2) for Er^{3+}, and ^4I_J (J = 11/2−15/2) for Nd^{3+} are situated energetically above the relaxation path of the emissive state, significantly reducing the possibilities of a nonradiative relaxation channel. As depicted in Scheme 1C, the Ln-centered (Ho^{3+}, Er^{3+}, and Nd^{3+}) emission becomes the predominant channel over nonradiative decay and the cycloaddition reaction, due to the presence of efficient IC-driven EnT and inefficient reverse EnT.

Finally, Scheme 1D represents the scenario of a cycloaddition reaction, applicable to most Ln^{3+} ions except Eu^{3+}, Ho^{3+}, Er^{3+}, and Nd^{3+}. These ions either possess higher (Sm^{3+}, $^4G_{5/2}$; Gd^{3+}, $^6P_{7/2}$; Tb^{3+}, $^5D_4$; Dy^{3+}, $^4F_{9/2}$) or lower (Ce^{3+}, $^2F_{7/2}$; Dy^{3+}, $^6F_{3/2}$; Yb^{3+}, $^2F_{5/2}$) excited-states levels compared to the resonant energy-crossing level (Scheme 1E). Without energy degenerate crossing, both ISC- and IC-driven EnT processes function as futile decay channels. Consequently, the ligand-centered ISC $^1\pi\pi^* \rightarrow {}^3\pi\pi^*$ becomes predominant, leading to the [4 + 4] photocycloaddition reaction by surpassing the moderate barrier (<10 kcal mol^{-1}). For the **1-Tb** complex, the calculated barrier height meets this criterion (ΔE = 9.1 kcal mol^{-1}, ΔG = 7.5 kcal mol^{-1}). The upper limit for the photocycloaddition rate (k_{cyc}) is estimated at 1.9×10^7 s^{-1}, competing with the characteristic fluorescence emission from the minimum of the delocalized excimer ($k_F = 1.4 \times 10^7$ s^{-1}). Thus, the characteristic emissions around 530 nm observed in **1-La**, **1-Ce**, **1-Sm**, **1-Gd**, **1-Tb**, **1-Dy**, and **1-Yb** can be considered indicative of the [4 + 4] photocycloaddition reaction. For the unique case of the **1-Yb** compound, excimer emission, metal luminescence, and photoreaction are all observed. The competitive coexistence of multiple excited state processes indicates a more complicated sensitization mechanism for Yb. The highly efficient excimer emission and photocycloaddition reaction indicate a very low efficiency of direct energy transfer from the ligand level to the emissive $^2F_{5/2}$ state of Yb^{3+} ion consistent with their relatively large energy gap. Of course, an unidentified low-energy excited state might operate as a channel to account for the Yb-centered emission, which will be further studied in our future work.

CONCLUSIONS

In summary, the photophysical and photochemical behavior of **1-Ln** complexes, incorporating an anthracene-based light-harvesting group, was thoroughly investigated using a multidisciplinary approach. Correlated and relativistic quantum chemical calculations, crystal engineering through photocycloaddition, and spectroscopic techniques were employed to elucidate the dependence of these processes on the Ln^{3+} ion. The innovative internal conversion-driven energy transfer (IC-EnT) theory, accompanied by three models, was developed to explain the differentiated dynamic behavior of Ln^{3+} ions in terms of luminescence and reactions, specifically considering the existence of efficient or futile energy resonant crossing. For lanthanide complexes with light-harvesting antenna of

https://doi.org/10.1021/jacsau.4c00540
JACS Au 2024, 4, 3606−3618

anthracene, a sensitive energy resonant crossing region exists, in which the ligand-to-metal EnT operates efficiently for energetically matched Ln^{3+} ions (Eu^{3+}, Ho^{3+}, Nd^{3+}, and Er^{3+}). However, in the unique case of the **1-Eu** complex, the crossing between its metal-centered emissive level and ground state sublevels significantly quenched red photoluminescence due to efficient reverse EnT. In scenarios without energy resonant crossing (**1-La**, **1-Ce**, **1-Sm**, **1-Gd**, **1-Tb**, **1-Dy**, and **1-Yb**), the stepwise [4 + 4] photocycloaddition reaction prevailed over metal-centered emission, although it competed with ligand-centered excimer emission.

The IC-EnT model introduced in this study complements the previously proposed ISC-controlled EnT approach, contributing to a universal theory for understanding lanthanide ion-regulated photophysical and photochemical processes. Integration of insights from these models offers a comprehensive understanding of the intricate dynamics in lanthanide systems, enabling the rational design of materials with tailored photophysical and photochemical properties. Our multidisciplinary approach highlights the potency of integrating theoretical calculations, crystal engineering, and spectroscopic techniques, advancing our understanding of lanthanide ion-regulated photophysical and photochemical processes.

■ ASSOCIATED CONTENT

Supporting Information

The Supporting Information is available free of charge at https://pubs.acs.org/doi/10.1021/jacsau.4c00540.

Experimental and computational details, crystallographic details, and full characterizations (SC-XRD, PXRD, IR, UV−vis and photoluminescence spectra, thermal analysis, photographs) of all described compounds, and CCDC 2233109−2233122 (PDF)

■ AUTHOR INFORMATION

Corresponding Authors

Li-Min Zheng − *State Key Laboratory of Coordination Chemistry, School of Chemistry and Chemical Engineering, Collaborative Innovation Centre of Advanced Microstructures, Nanjing University, Nanjing 210023, P. R. China;* orcid.org/0000-0003-4437-1105; Email: lmzheng@nju.edu.cn

Michael Dolg − *Key Laboratory of Theoretical and Computational Photochemistry of the Chinese Ministry of Education, College of Chemistry, Beijing Normal University, Beijing 100875, P. R. China; Theoretical Chemistry, University of Cologne, 50939 Cologne, Germany;* orcid.org/0000-0002-0538-0837; Email: m.dolg@uni-koeln.de

Xuebo Chen − *Key Laboratory of Theoretical and Computational Photochemistry of the Chinese Ministry of Education, College of Chemistry, Beijing Normal University, Beijing 100875, P. R. China;* orcid.org/0000-0002-9814-9908; Email: xuebochen@bnu.edu.cn

Authors

Liangliang Wu − *Key Laboratory of Theoretical and Computational Photochemistry of the Chinese Ministry of Education, College of Chemistry, Beijing Normal University, Beijing 100875, P. R. China; Advanced Institute of Natural Sciences, Beijing Normal University, Zhuhai 519087, P. R. China;* orcid.org/0000-0002-5434-0786

Xin-Da Huang − *State Key Laboratory of Coordination Chemistry, School of Chemistry and Chemical Engineering, Collaborative Innovation Centre of Advanced Microstructures, Nanjing University, Nanjing 210023, P. R. China*

Weijia Li − *Key Laboratory of Theoretical and Computational Photochemistry of the Chinese Ministry of Education, College of Chemistry, Beijing Normal University, Beijing 100875, P. R. China*

Xiaoyan Cao − *Key Laboratory of Theoretical and Computational Photochemistry of the Chinese Ministry of Education, College of Chemistry, Beijing Normal University, Beijing 100875, P. R. China; Theoretical Chemistry, University of Cologne, 50939 Cologne, Germany;* orcid.org/0000-0002-3438-575X

Wei-Hai Fang − *Key Laboratory of Theoretical and Computational Photochemistry of the Chinese Ministry of Education, College of Chemistry, Beijing Normal University, Beijing 100875, P. R. China;* orcid.org/0000-0002-1668-465X

Complete contact information is available at: https://pubs.acs.org/10.1021/jacsau.4c00540

Author Contributions

[⊥]L.W., X.-D.H., and W.L. contributed equally to this work. X.C., L.Z., W.F., and M.D. conceived the ideas and organized the work. L.Z. and X.H. designed and performed the experimental studies. L.W., W.L., and X.C. performed theoretical calculations. All authors contributed to data analysis and interpretation. X.C., L.Z., and M.D. wrote the manuscript with input from coauthors. All authors read and commented on the manuscript.

Notes

The authors declare no competing financial interest.

■ ACKNOWLEDGMENTS

This work was supported by grants from the National Natural Science Foundation of China (22120102005, 22273037, and 22303007), Major Project of National Natural Science Foundation of China (22393914), and National Key R&D Program of China (2022YFB3603001).

■ REFERENCES

(1) Ramamurthy, V.; Venkatesan, K. Photochemical reactions of organic crystals. *Chem. Rev.* **1987**, *87*, 433−481.

(2) Schmidt, G. M. J. Photodimerization in the solid state. *Pure Appl. Chem.* **1971**, *27*, 647−678.

(3) (a) Bouas-Laurent, H.; Castellan, A.; Desvergnea, J.-P.; Lapouyade, R. Photodimerization of anthracenes in fluid solution: structural aspects. *Chem. Soc. Rev.* **2000**, *29*, 43−55. (b) Bouas-Laurent, H.; Castellan, A.; Desvergnea, J.-P.; Lapouyade, R. Photodimerization of anthracenes in fluid solutions: (part 2) mechanistic aspects of the photocycloaddition and of the photochemical and thermal cleavage. *Chem. Soc. Rev.* **2001**, *30*, 248−263. (c) Christensen, P. R.; Patrick, B. O.; Caron, É.; Wolf, M. O. Oxidation-State-Dependent Photochemistry of Sulfur-Bridged Anthracenes. *Angew. Chem., Int. Ed.* **2013**, *52*, 12946−12950. (d) Kislyak, A.; Frisch, H.; Gernhardt, M.; Steenberge, P. H. M. V.; D'hooge, D. R.; Barner-Kowollik, C. Time-Dependent Differential and Integral Quantum Yields for Wavelength-Dependent [4 + 4] Photocycloadditions. *Chem. - Eur. J.* **2020**, *26*, 478−484.

(4) (a) Kim, T.; Zhu, L.; Al-Kaysi, R. O.; Bardeen, C. J. Organic photomechanical materials. *ChemPhysChem* **2014**, *15*, 400−414.

(b) Naumov, P.; Chizhik, S.; Panda, M. K.; Nath, N. K.; Boldyreva, E. Mechanically Responsive Molecular Crystals. *Chem. Rev.* **2015**, *115*, 12440−12490. (c) Huang, C.; Huang, R.; Zhang, S.; Sun, H.; Wang, H.; Du, B.; Xiao, Y.; Yu, T.; Huang, W. Recent Development of Photodeformable Crystals: From Materials to Mechanisms. *Research* **2021**, *2021*, No. 9816535. (d) Hino, Y.; Matsuo, T.; Hayashi, S. Structural Phase Transitions in Anthracene Crystals. *ChemPlusChem* **2022**, *87*, No. e202200157.

(5) (a) Feng, X.; Schlüter, A. D. Towards macroscopic crystalline 2D polymers. *Angew. Chem., Int. Ed.* **2018**, *57*, 13748−13763. (b) Paderes, M. C.; Diaz, M. J.; Pagtalunan, C. A.; Bruzon, D. A.; Tapang, G. A. Photo-Controlled [4 + 4] Cycloaddition of Anthryl-Polymer Systems: A Versatile Approach to Fabricate Functional Materials. *Chem. - Asian J.* **2022**, *17*, No. e202200193. (c) Sun, C.; Oppenheim, J. J.; Skorupskii, G.; Yang, L.; Dincă, M. Reversible Topochemical Polymerization and Depolymerization of a Crystalline 3D Porous Organic Polymer with C−C Bond Linkages. *Chem* **2022**, *8*, 3215−3224.

(6) (a) Liu, W.; Guo, L.; Fan, Y.; Huang, Z.; Cong, H. [4 + 4] Photodimerization of Anthracene Derivatives: Recent Synthetic Advances and Applications. *Chin. J. Org. Chem.* **2017**, *37*, 543−554. (b) Wang, H.; Liu, F.; Helgeson, R. C.; Houk, K. N. Reversible photochemically gated transformation of a hemicarcerand to a carcerand. *Angew. Chem., Int. Ed.* **2013**, *52*, 655−659. (c) Gole, B.; Kauffmann, B.; Tron, A.; Maurizot, V.; McClenaghan, N.; Huc, I.; Ferrand, Y. Selective and Cooperative Photocycloadditions within Multistranded Aromatic Sheets. *J. Am. Chem. Soc.* **2022**, *144*, 6894−6906.

(7) (a) Huang, X.-D.; Xu, Y.; Fan, K.; Bao, S.-S.; Kurmoo, M.; Zheng, L.-M. Reversible SC-SC Transformation involving [4 + 4] Cycloaddition of Anthracene: A Single-Ion to Single-Molecule Magnet and Yellow-Green to Blue-White Emission. *Angew. Chem., Int. Ed.* **2018**, *57*, 8577−8581. (b) Huang, X.-D.; Wen, G.-H.; Bao, S.-S.; Jia, J.-G.; Zheng, L.-M. Thermo- and light-triggered reversible interconversion of dysprosium−anthracene complexes and their responsive optical, magnetic and dielectric properties. *Chem. Sci.* **2021**, *12*, 929−937. (c) Huang, X.-D.; Ma, X.-F.; Shang, T.; Zhang, Y.-Q.; Zheng, L.-M. Photocontrollable Magnetism and Photoluminescence in a Binuclear Dysprosium Anthracene Complex. *Inorg. Chem.* **2023**, *62*, 1864−1874. (d) Huang, X.-D.; Ma, X.-F.; Zheng, L.-M. Photo-responsive Single-Molecule Magnet Showing 0D to 1D Single-Crystal-to-Single-Crystal Structural Transition and Hysteresis Modulation. *Angew. Chem., Int. Ed.* **2023**, *62* (15), No. e202300088. (e) Huang, X.-D.; Hong, B.-K.; Wen, G.-H.; Li, S.-H.; Zheng, L.-M. Photo-controllable heterostructured crystals of metal−organic frameworks via reversible photocycloaddition. *Chem. Sci.* **2023**, *14*, 1852−1860.

(8) (a) Castellano, M.; Ferrando-Soria, J.; Pardo, E.; Julve, M.; Lloret, F.; Mathonière, C.; Pasán, J.; Ruiz-Pérez, C.; Cañadillas-Delgado, L.; Ruiz-García, R.; Cano, J. Photoswitching of the Antiferromagnetic Coupling in an Oxamato-Based Dicopper(II) Anthracenophane. *Chem. Commun.* **2011**, *47*, 11035−11037. (b) Yu, Q.; Li, M.; Gao, J.; Xu, P.; Chen, Q.; Xing, D.; Yan, J.; Zaworotko, M.; Xu, J.; Chen, Y.; Cheng, P.; Zhang, Z. Fabrication of Large Single Crystals for Platinum-Based Linear Polymers with Controlled-Release and Photoactuator Performance. *Angew. Chem., Int. Ed.* **2019**, *58*, 18634−18640. (c) Ma, Y.-J.; Xiao, G.; Fang, X.; Chen, T.; Yan, D. Leveraging Crystalline and Amorphous States of a Metal-Organic Complex for Transformation of the Photosalient Effect and Positive-Negative Photochromism. *Angew. Chem., Int. Ed.* **2023**, *62*, No. e202217054.

(9) (a) Rocha, J.; Carlos, L. D.; Paz, F. A. A.; Ananias, D. Luminescent multifunctional lanthanides-based metal−organic frameworks. *Chem. Soc. Rev.* **2011**, *40*, 926−940. (b) Salerno, E. V.; Eliseeva, S. V.; Schneider, B. L.; Kampf, J. W.; Petoud, S.; Pecoraro, V. L. Visible, Near-Infrared, and Dual-Range Luminescence Spanning the 4f Series Sensitized by a Gallium(III)/Lanthanide(III) Metallacrown Structure. *J. Phys. Chem. A* **2020**, *124*, 10550−10564.

(10) (a) Zhang, Q. Q.; Wu, L. L.; Cao, X. Y.; Chen, X. B.; Fang, W. H.; Dolg, M. Energy Resonance Crossing Controls the Photoluminescence of Europium Antenna Probes. *Angew. Chem., Int. Ed.* **2017**, *56*, 7986−7990. (b) Wu, L. L.; Fang, Y.; Zuo, W. L.; Wang, J. J.; Wang, J.; Wang, S. F.; Cui, Z. F.; Fang, W. H.; Sun, H. L.; Li, Y. L.; Chen, X. B. Excited-State Dynamics of Crossing-Controlled Energy Transfer in Europium Complexes. *JACS Au* **2022**, *2*, 853−864.

(11) Kitagawa, Y.; Naito, A.; Aikawa, K.; Shima, K.; Shoji, S.; Fushimi, K.; Hasegawa, Y. Tribo-Excited Chemical Reaction Using an EuIII Complex with a Stacked Anthracene Framework. *Chem. - Eur. J.* **2022**, *28*, No. e202104401.

(12) (a) Weissman, S. I. Intramolecular Energy Transfer The Fluorescence of Complexes of Europium. *J. Chem. Phys.* **1942**, *10*, 214−217. (b) Eliseeva, S. V.; Bünzli, J.-C. G. Lanthanide luminescence for functional materials and bio-sciences. *Chem. Soc. Rev.* **2010**, *39*, 189−227. (c) Bünzli, J.-C. On the design of highly luminescent lanthanide complexes. *Coord. Chem. Rev.* **2015**, *293*−*294*, 19−47. (d) Bünzli, J.-C. Lanthanide Luminescence for Biomedical Analyses and Imaging. *Chem. Rev.* **2010**, *110*, 2729−2755. (e) Heffern, M. C.; Matosziuk, L. M.; Meade, T. J. Lanthanide Probes for Bioresponsive Imaging. *Chem. Rev.* **2014**, *114*, 4496−4539. (f) Moore, E. G.; Samuel, A. P. S.; Raymond, K. N. From Antenna to Assay: Lessons Learned in Lanthanide Luminescence. *Acc. Chem. Res.* **2009**, *42*, 542−552. (g) Bünzli, J. G. Rising Stars in Science and Technology: Luminescent Lanthanide Materials. *Eur. J. Inorg. Chem.* **2017**, *2017*, 5058−5063. (h) Monteiro, J. H. S. K.; De Bettencourt-Dias, A.; Sigoli, F. A. Estimating the Donor-Acceptor Distance to Tune the Emission Efficiency of Luminescent Lanthanide Compounds. *Inorg. Chem.* **2017**, *56*, 709−712. (i) Latva, M.; Takalo, H.; Mukkala, V. M.; Matachescu, C.; RodriguezUbis, J. C.; Kankare, J. Correlation between the lowest triplet state energy level of the ligand and lanthanide(III) luminescence quantum yield. *J. Lumin.* **1997**, *75*, 149−169.

(13) da Rosa, P. P. F.; Kitagawa, Y.; Hasegawa, Y. Luminescent lanthanide complex with seven-coordination geometry. *Coord. Chem. Rev.* **2020**, *406*, No. 213153.

(14) (a) Binnemans, K. Interpretation of europium(III) spectra. *Coord. Chem. Rev.* **2015**, *295*, 1−45. (b) Ward, M. D. Mechanisms of sensitization of lanthanide(III)-based luminescence in transition metal/lanthanide and anthracene/lanthanide dyads. *Coord. Chem. Rev.* **2010**, *254*, 2634−2642.

(15) (a) Daumann, L. J.; Tatum, D. S.; Snyder, B. E.; Ni, C.; Law, G.-l.; Solomon, E. I.; Raymond, K. N. New Insights into Structure and Luminescence of Eu^{III} and Sm^{III} Complexes of the 3,4,3-LI(1,2-HOPO) Ligand. *J. Am. Chem. Soc.* **2015**, *137*, 2816−2819. (b) de Sá, G.; Malta, O. L.; Donegá, C. D.; Simas, A. M.; Longo, R. L.; Santa-Cruz, P. A.; da Silva, E. F. Spectroscopic properties and design of highly luminescent lanthanide coordination complexes. *Coord. Chem. Rev.* **2000**, *196*, 165−195. (c) Pacold, J. I.; Tatum, D. S.; Seidler, G. T.; Raymond, K. N.; Zhang, X.; Stickrath, A. B.; Mortensen, D. R. Direct Observation of 4f Intrashell Excitation in Luminescent Eu Complexes by Time-Resolved X-ray Absorption Near Edge Spectroscopy. *J. Am. Chem. Soc.* **2014**, *136*, 4186−4191. (d) Mara, M. W.; Tatum, D. S.; March, A.-M.; Doumy, G.; Moore, E. G.; Raymond, K. N. Energy Transfer from Antenna Ligand to Europium(III) Followed Using Ultrafast Optical and X-ray Spectroscopy. *J. Am. Chem. Soc.* **2019**, *141*, 11071−11081. (e) Tanner, P. A.; Zhou, L.; Duan, C.; Wong, K.-L. Misconceptions in electronic energy transfer: bridging the gap between chemistry and physics. *Chem. Soc. Rev.* **2018**, *47*, 5234−5265.

(16) Sveshnikova, E. B.; Ermolaev, V. L. Inductive-resonant theory of nonradiative transitions in lanthanide and transition metal ions. *Opt. Spectrosc.* **2011**, *111*, 34−50.

(17) Horrocks, W. D.; Bolender, J. P.; Smith, W. D.; Supkowski, R. M. Photosensitized Near Infrared Luminescence of Ytterbium(III) in Proteins and Complexes Occurs via an Internal Redox Process. *J. Am. Chem. Soc.* **1997**, *119*, 5972−5973.

(18) *Program for Data Extraction and Reduction, Siemens Analytical X-ray Instruments*; SAINT: Madison, WI, 1994−1996.

https://doi.org/10.1021/jacsau.4c00540
JACS Au 2024, 4, 3606−3618

(19) Krause, L.; Herbst-Irmer, R.; Sheldrick, G. M.; Stalke, D. Comparison of silver and molybdenum microfocus X-ray sources for single-crystal structure determination. *J. Appl. Crystallogr.* **2015**, *48*, 3−10.
(20) Sheldrick, G. M. Crystal structure refinement with SHELXL. *Acta Crystallogr., Sect. C: Struct. Chem.* **2015**, *71*, 3−8.
(21) (a) Dolg, M.; Cao, X. Y. Relativistic Pseudopotentials: Their Development and Scope of Applications. *Chem. Rev.* **2012**, *112*, 403−480. (b) Dolg, M.; Stoll, H.; Preuß, H. Energy-adjusted ab initio pseudopotentials for the rare earth elements. *J. Chem. Phys.* **1989**, *90*, 1730−1734. (c) Dolg, M.; Stoll, H.; Savin, A.; Preuß, H. Energy-adjusted pseudopotentials for the rare earth elements. *Theor. Chim. Acta* **1989**, *75*, 173−194. (d) Cao, X.; Dolg, M. Valence basis sets for relativistic energy-consistent small-core lanthanide pseudopotentials. *J. Chem. Phys.* **2001**, *115*, 7348−7355.
(22) Frisch, M. J.; Trucks, G. W.; Schlegel, H. B.; Scuseria, G. E.; Robb, M. A.; Cheeseman, J. R.; Montgomery, J. A., Jr.; Vreven, T.; Kudin, K. N.; Burant, J. C.; Millam, J. M.; Iyengar, S. S.; Tomasi, J.; Barone, V.; Mennucci, B.; Cossi, M.; Scalmani, G.; Rega, N.; Petersson, G. A.; Nakatsuji, H.; Hada, M.; Ehara, M.; Toyota, K.; Fukuda, R.; Hasegawa, J.; Ishida, M.; Nakajima, T.; Honda, Y.; Kitao, O.; Nakai, H.; Klene, M.; Li, X.; Knox, J. E.; Hratchian, H. P.; Cross, J. B.; Bakken, V.; Adamo, C.; Jaramillo, J.; Gomperts, R.; Stratmann, R. E.; Yazyev, O.; Austin, A. J.; Cammi, R.; Pomelli, C.; Ochterski, J. W.; Ayala, P. Y.; Morokuma, K.; Voth, G. A.; Salvador, P.; Dannenberg, J. J.; Zakrzewski, V. G.; Dapprich, S.; Daniels, A. D.; Strain, M. C.; Farkas, O.; Malick, D. K.; Rabuck, A. D.; Raghavachari, K.; Foresman, J. B.; Ortiz, J. V.; Cui, Q.; Baboul, A. G.; Clifford, S.; Cioslowski, J.; Stefanov, B. B.; Liu, G.; Liashenko, A.; Piskorz, P.; Komaromi, I.; Martin, R. L.; Fox, D. J.; Keith, T.; Al-Laham, M. A.; Peng, C. Y.; Nanayakkara, A.; Challacombe, M.; Gill, P. M. W.; Johnson, B.; Chen, W.; Wong, M. W.; Gonzalez, C.; Pople, J. A. *Gaussian 03*, Revision D.02; Gaussian, Inc.: Wallingford, CT, 2004.
(23) Karlstrøm, G.; Lindh, R.; Malmqvist, P.-Å.; Roos, B. O.; Ryde, U.; Veryazov, V.; Widmark, P.-O.; Cossi, M.; Schimmelpfennig, B.; Neogrady, P.; Seijo, L. MOLCAS: a program package for computational chemistry. *Comput. Mater. Sci.* **2003**, *28*, 222−239.
(24) (a) Yatsimirskii, K. B.; Davidenko, N. K. Absorption spectra and structure of lanthanide coordination compounds in solution. *Coord. Chem. Rev.* **1979**, *27*, 223−273. (b) Carnall, W. T.; Fields, P. R.; Rajnak, K. Spectral Intensities of the Trivalent Lanthanides and Actinides in Solution. II. Pm^{3+}, Sm^{3+}, Eu^{3+}, Gd^{3+}, Tb^{3+}, Dy^{3+}, and Ho^{3+}. *J. Chem. Phy.* **1968**, *49*, 4412−4423. (c) Walsh, B. M.; Barnes, N. P.; Bartolo, B. D. Branching ratios, cross sections, and radiative lifetimes of rare earth ions in solids: Application to Tm^{3+} and Ho^{3+} ions in $LiYF_4$. *J. Appl. Phys.* **1998**, *83*, 2772−2787.
(25) (a) Liu, H.-C.; Gao, Y.; Yang, B. High-efficiency dimer fluorescence system based on $\pi-\pi$ interaction between anthracenes: Recognition of excimer. *Chin. Sci. Bull.* **2017**, *62*, 4099−4112. (b) Liu, J.-C.; Huang, X.-D.; Zou, Q.; Bao, S.-S.; Wang, X.-Z.; Ma, J.-Y.; Zheng, L.-M. Synergetic magnetic and luminescence switching via solid state phase transitions of the dysprosium−dianthracene complex. *J. Mater. Chem. C* **2020**, *8*, 7369−7377.
(26) Osawa, M.; Hoshino, M.; Wada, T.; Hayashi, F.; Osanai, S. Intra-Complex Energy Transfer of Europium(III) Complexes Containing Anthracene and Phenanthrene Moieties. *J. Phys. Chem. A* **2009**, *113*, 10895−10902.
(27) Krekić, K.; Klintuch, D.; Lescop, C.; Calvez, G.; Pietschnig, R. Structural and Luminescence Properties of Anthracene- and Biphenyl-Based Lanthanide Bisphosphonate Ester Coordination Polymers. *Inorg. Chem.* **2019**, *58*, 382−390.
(28) Kislyak, A.; Frisch, H.; Gernhardt, M.; Van Steenberge, P. H. M.; D'hooge, D. R.; Barner-Kowollik, C. Time-Dependent Differential and Integral Quantum Yields for Wavelength-Dependent [4 + 4] Photocycloadditions. *Chem. - Eur. J.* **2020**, *26*, 478−484.
(29) Bunzli, J. C. G.; Froidevaux, P.; Harrowfield, J. M. Complexes of lanthanoid salts with macrocyclic ligands. 41. Photophysical properties of lanthanide dinuclear complexes with p-tert-butylcalix[8]-arene. *Inorg. Chem.* **1993**, *32*, 3306−3311.

https://doi.org/10.1021/jacsau.4c00540
JACS Au 2024, 4, 3606−3618